Author's personal copy

Solid State Communications 152 (2012) 1404–1410

Contents lists available at SciVerse ScienceDirect

Solid State Communications

journal homepage: www.elsevier.com/locate/ssc

Quantum transport in disordered graphene: A theoretical perspective

Stephan Roche [a,b,*], Nicolas Leconte [c], Frank Ortmann [a], Aurélien Lherbier [c], David Soriano [a], Jean-Christophe Charlier [c]

[a] CIN2 (ICN-CSIC) and Universitat Autónoma de Barcelona, Catalan Institute of Nanotechnology, Campus UAB, 08193 Bellaterra (Barcelona), Spain
[b] ICREA, Institució Catalana de Recerca i Estudis Avançats, 08070 Barcelona, Spain
[c] Université catholique de Louvain (UCL), Institute of Condensed Matter and Nanosciences (IMCN), NAPS-ETSF, 8 chemin des étoiles, 1348 Louvain-la-Neuve, Belgium

ARTICLE INFO

Article history:
Accepted 12 April 2012
Accepted by L. Brey
Available online 21 April 2012

Keywords:
A. Disordered graphene
D. Quantum transport
D. Metal–insulator transition
E. Numerical simulations

ABSTRACT

The present theoretical review puts into perspective simulations of quantum transport properties in disordered graphene-based materials. In particular, specific effects induced by short versus long range scattering on the minimum conductivity, weak (anti-)localization, and strongly insulating regimes are discussed in depth. Using various types of disorder profiles (random fluctuations of the local impurity potential, long range Coulomb scatterers or more intrusive chemical functionalizations), universal aspects of transport as well as novel features in chemically modified graphene-based materials are depicted, especially in the cases of oxygen and hydrogen atoms adsorption. Finally, our theoretical results are compared to experimental measurements.

© 2012 Elsevier Ltd. All rights reserved.

1. Introduction

Graphene was discovered in 2004 in Manchester University [1–3] after years of attempts to produce few layers graphite using epitaxial growth or mechanical cleavage. Novel type of electronic excitations (so-called *massless Dirac Fermions*) [4,5] have been unveiled in this two-dimensional atom-thick layer, and the advent of graphene-based technologies has become an emerging reality [6]. Low-energy electronic states encompass a new quantum degree of freedom (pseudospin) which yields a wealth of anomalous transport features such as Klein tunneling [7], including supercollimation which is a new way of guiding charge flows [8], weak antilocalization [9–11], and the unconventional quantum Hall effect [12,13].

Such unique transport features are however strongly dependent on the nature of intrinsic and extrinsic disorders, and detrimental effects of graphene damaging can actually be transformed into advantages such as the engineering of mobility gaps or novel functionalities of graphene devices [14,15]. To date, the precise relationship between the underlying disorder features and the existence of graphene's unique transport properties remains however elusive and fiercely debated.

One key issue, strongly dependent on the disorder nature, is the role of pseudospin effects in modulating conductance fingerprints in graphene-based materials. Indeed, in ordinary disordered materials, quantum interferences between multiple scattering paths produce a quantum correction to the semiclassical (Drude) conductivity. This correction can either reduce (weak localization-WL) [16], or enhance (weak antilocalization-WAL) [17,18] the conductivity. WAL usually originates from strong spin-orbit coupling, which is actually very weak in flat graphene. However, Suzuura and Ando [19] first suggested that in graphene, *even in the absence of spin–orbit coupling*, WAL would occur depending on the impurity potential range and related disruption of AB sublattice symmetry. A complete perturbation (diagrammatic) theory was further developed by McCann and coworkers [9], to evaluate the quantum correction to the semiclassical (Drude) result. To compute such Cooperon correction within the scheme of perturbation theory, several phenomenological parameters were introduced to distinguish between different diagrams either conveyed by *intravalley or intervalley scattering events*. The corresponding scattering times fix the onset of Cooperon corrections, or equivalently fix the length scales at which quantum interferences in scattering trajectories become appreciable. It is however difficult, if not impossible, to evaluate those somewhat generic parameters for a given realistic microscopic disorder model. Besides, experimental evidences of WAL have been reported [10,11], together with a complex phase diagram, showing multiple crossovers from WAL (negative magnetoconductance) to WL (positive magnetoconductance) when tuning the energy of charge carriers or the sample temperature [10,11]. Notwithstanding, the agreement between the diagrammatic theory [9] and the experiments [10,11] remains qualitative, with elusive connection to the detail of the microscopic disorder driving such crossovers.

The full understanding of the microscopical origin of such a complex phase diagram and its relation to a possible metal–insulator

* Corresponding author at: CIN2 (ICN-CSIC) and Universitat Autónoma de Barcelona, Catalan Institute of Nanotechnology, Campus UAB, 08193 Bellaterra (Barcelona), Spain.
E-mail address: stephan.roche@icn.cat (S. Roche).

0038-1098/$ - see front matter © 2012 Elsevier Ltd. All rights reserved.
http://dx.doi.org/10.1016/j.ssc.2012.04.030

Author's personal copy

transition thus remains to be established in details. In that perspective, it is crucial to clarify the connection between the atomic-scale disorder features and the magnetic-field dependent quantum interference effects (QIEs) driving the conductance modulations, as well as the true contribution of the pseudospin degree of freedom. Finally, whereas weak localization in 2D is a precursor of a truly insulating state in the zero temperature limit [20–23], WAL points towards a robust metallic state, a fact in sharp contrast with the usual scaling theory of localization for two-dimensional disordered systems [16].

Transport properties in graphene-based systems are strongly dependent on the nature of possible sources of disorder. Strong disorder can be obtained for instance when irradiating graphene samples, which produces structural defects [24,27,28] (or even an amorphous graphene structure) [29]. Graphene can be made even more disordered, and starts loosing its sp^2 electronics integrity when undergoing oxidation [30,31] or hydrogenation [33]. Some universalities in transport scaling behavior for disordered graphene in the presence of resonant scatters have been reported using the renormalization group theory or full counting statistics [25,26]. All these chemical modifications processes are strongly invasive for electronic and transport properties and systematically drive the system to a strong Anderson insulator [32]. The recent observation of an Anderson localization in high-mobility graphene sandwiched in between two boron-nitride layers is in that respect puzzling and demands for in-depth inspection [34].

This paper is organized as follows. Section 2 first outlines the Kubo formalism which is used to study the various transport regimes occurring in disordered graphene. A real-space order-N implementation combined with state-of-the art first principles calculations provides an efficient tool for quantitative analysis of transport in complex chemically disordered graphene structures with very large system sizes. Then, in the first part of Section 3, the effect of short range disorder is discussed using the Anderson disorder model, a generic approach for studying localization phenomena in condensed matter [16]. In the second part, the microscopic origin of the crossover from WAL to WL will be unraveled. Further, in Section 4, the effect of adsorbed oxygen will be shown to allow certain tunability of transport features from a metallic to an insulating case (either by varying the carriers energy, the temperature or the system size), whereas partial hydrogenation will unveil an unprecedented and deep connection between the formation of local ferromagnetic ordering and the total suppression of localization phenomena.

2. Order-N real-space Kubo–Greenwood quantum transport methodology

To investigate quantum transport in disordered graphene, a real-space order-N numerical implementation within the Kubo–Greenwood formalism is employed [35–41]. Within this approach, the diffusion coefficient $D_x(E,t)$ in the transport direction x is calculated at each time step using $D_x(E,t)=\Delta X^2(E,t)/t$ where

$$\Delta X^2(E,t)=\frac{Tr[[\hat{X},\hat{U}(t)]^{\dagger}\delta(E-\hat{H})[\hat{X},\hat{U}(t)]]}{Tr[\delta(E-\hat{H})]} \quad (1)$$

with $\hat{U}(t)=e^{-i\hat{H}t/\hbar}$, the time-evolution operator. The latter can be expanded using Chebyshev polynomials and both the numerator and denominator in Eq. (1) are calculated recursively using *continued fractions* expansions (Lanczos method [42]). The termination term is typically applied after a few hundreds of recursion steps. Finally, the trace is replaced by the average of about 10 random phase states, a trick which greatly reduce the computational cost, allowing the study of huge system sizes [35–39,41]. As a matter of fact, simulations of charge mobility in disordered graphene samples can be achieved for systems with several tens of millions of atomic orbitals (typical graphene area of 1 μm^2). Similar methodology has been also recently developed for following phonon propagation in the harmonic approximation and computing the associated thermal conductivity of material of any complexity [43–45].

Assuming the system is isotropic for the in-plane x and y directions, the 2D diffusion coefficient reads as $D(t)=D_x(t)+D_y(t)=2D_x(t)$. From the diffusion coefficient, the mean free path $\ell_e(E)$ and the semiclassical conductivity $\sigma_{sc}(E)$ can be calculated using respectively $\ell_e(E)=D^{max}(E)/2\nu(E)$ and $\sigma_{sc}(E)=\frac{1}{4}e^2\rho(E)D^{max}(E)$ with $\nu(E)$ the carrier velocity, D^{max} the maximum value of $D(t)$, e the electronic charge, and $\rho(E)$ the density of states (DOS). The semiclassical Kubo conductivity is compared with the values obtained with the Drude approximation close to the Dirac point $\sigma_D(E)=(4e^2/h)k\ell_e(E)/2$ using $E=\hbar\nu_F k$ with $\nu_F\sim 10^6$ m s^{-1} the massless Dirac fermions velocity in pristine graphene.

3. Short range versus long range disorder potentials

The nature and impact of disorder in graphene has been a long debated issue. Firstly, because of the different fabrication techniques to obtain graphene inducing either local or more long range lattice imperfections (defects, impurities, ripples and long range strain deformations, etc.) and secondly, because of the possibility to observe unique transport features such as Klein tunneling, electron collimation or weak antilocalization phenomena.

Klein tunneling in graphene [7] is a spectacular manifestation of the Dirac fermions physics where backward reflection is partially or totally suppressed (depending on the incident angle of the incoming wavepacket and the height and width of the barrier) when charge crosses a tunneling barrier. This result contrasts with usual behavior in Schrödinger physics for which the quantum wavepackets are exponentially damped when crossing a barrier of increasing width. Klein tunneling is thus an efficient mechanism to suppress localization effects provided the impurity potential is sufficiently long range to prohibit intervalley scattering between the two inequivalent Dirac cones, and therefore allows only intravalley-mediated scattering trajectories. It roots in the approximately symmetric electron–hole electronic band structure and the pseudospin degree of freedom associated to the AB sublattice degeneracy. Note that a similar mechanism has been previously well documented in metallic carbon nanotubes [46–49] where total suppression of backscattering appears in this one-dimensional case.

Pseudospin shares similar symmetries with the spin degree of freedom, and as such, the corresponding wavefunctions acquires an extra phase factor (Berry phase) which can provoke additional interferences under certain circumstances. The observation of the weak antilocalization (WAL) in graphene [10,11] is such a manifestation of pseudospin effects on phase interferences. WAL in graphene has been rigorously worked out by McCann and coworkers [9], who provide a solid theoretical foundation of a constructive interferences effect between diffusive states propagating clockwise and anticlockwise along a trajectory back to some origin, and monitored by pseudospin-related phase factors. Again, the nature of disorder and contribution of intravalley versus intervalley scattering events is key in understanding crossover regimes between WL and WAL regimes. The possibility of strong (Anderson) localization is also inherent to the nature of disorder, and is expected to follow continuously the weak localization corrections, as dictated by the scaling theory of localization [16].

It is therefore of paramount importance to clarify the contribution of different possible sources of disorder in graphene and their impact on transport properties. Hereafter, we will consider

Author's personal copy

various cases from more academic (but generic) scattering potential such as the Anderson disorder, to long range scatterers (mimicking charged impurities), and to more invasive chemical defects such as adsorbed oxygen and hydrogen atoms. A more complete and comprehensive picture of transport phenomena in disordered graphene will then be disclosed.

3.1. Short range scattering

The case of a generic model for short range scattering potential, namely the Anderson disorder, is firstly considered. This white noise uncorrelated disorder is introduced through modulations of the onsite energies of a π-orbital tight-binding Hamiltonian ($\varepsilon_\pi = \varepsilon_\pi + \delta\varepsilon_\pi$). The disorder strength is tuned by choosing randomly $\delta\varepsilon_\pi \in [-W/2, W/2]\gamma_0$ energy perturbations with $\gamma_0 = -2.7$ eV the hopping term between nearest neighbor π-orbitals. This disorder could in principle mimic neutral impurities such as structural defects, dislocation lines, or adatoms, although the local geometry and chemical reactivity of defects and impurities actually demand for more sophisticated *ab initio* calculations if aiming at quantitative predictions (see Refs. [14,15,24,50] as illustrations). An interesting aspect of this model is however that numerical simulations can be contrasted to analytical results derived in the Self-Consistent Born Approximation (SCBA) [51,52]. Indeed, within SCBA, the semiclassical part of the conductivity (that is neglecting all interferences effects driven by Cooperon contributions) due to short range disorder is derived as [51]

$$\sigma_{sc}(E) = \frac{1}{2}\frac{e^2}{\pi^2\hbar}\left[\left(\frac{E-\Delta(E)}{\Gamma(E)} + \frac{\Gamma(E)}{E-\Delta(E)}\right)\arctan\frac{E-\Delta(E)}{\Gamma(E)} + 1\right]$$

with $\Delta(E) = \Re e\Sigma(E)$ and $\Gamma(E) = \Im m\Sigma(E)$ derived from the self-energy which satisfies the self-consistent energy equation

$$\Sigma(E+i\eta) = \frac{n_i u^2}{2\pi}(E-\Sigma(E+i\eta))\int_0^{k_c}\frac{kdk}{(E-\Sigma(E+i\eta))^2-(\gamma k)^2}$$

with n_i the defect density, u^2 the average squared disorder strength (a mapping of this model to the Anderson disorder is possible by adjusting parameters to obtain same average values and variances, i.e. $n_i(1-n_i)|u| = W_{\gamma_0}/\sqrt{12}$) and $k_c = \epsilon_c/\gamma_0$ the cut-off where $\epsilon_c = 50\epsilon_0$ in the simulations [46–49]. ϵ_0 is an arbitrary energy scale which is assumed to have the same order of magnitude as relevant energies such as E, Δ and Γ in the SCBA [51]. In the Boltzmann limit Δ=0 and $E/\Gamma_0 \gg 1$ the conductivity only depends on the dimensionless disorder parameter $A = 4\pi\gamma_0^2/n_i u^2$.

In addition to a specific energy dependence of $\sigma_{sc}(E)$, the value at the Dirac point $\sigma_{sc} = 4e^2/\pi h$ appears as a fundamental minimum limit. Using the Kubo method, we obtain σ_{sc} for various values of W as shown in Fig. 1. The agreement with SCBA results is highly convincing. For W=2, characterizing the scattering strength, the dimensionless parameter A is set to 21 to obtain a convincing fit for energies up to $2\epsilon_0$ with $\epsilon_0 = 0.3$ eV. For higher energies, the agreement with SCBA is lost due to higher order deviations. Also, for such disorder the SCBA is not sufficient as all symmetries are broken and the system is driven from a weak to strong localization regime as dictated by the scaling theory of localization in two-dimensional systems [16,41].

3.2. Long range scattering

To explore the possibility of crossovers between a weak localization to a weak antilocalization regime, we adopt a different disorder model, which describes a certain density of Coulomb impurities defined by a long range scattering potential [53,54]. The contributions from N_I impurities randomly distributed at position $\mathbf{r}_i$ (among N sites of the system) is given by renormalized

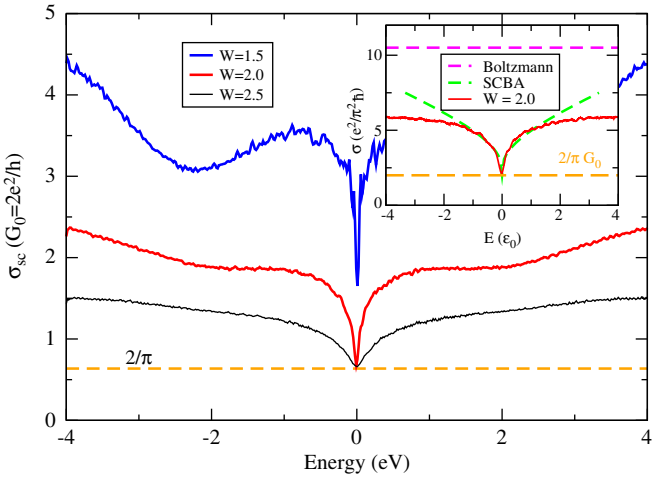

Fig. 1. (Color online) Main frame: energy-dependent semiclassical conductivity for Anderson disorder strengths of $W = 1.5$, 2.0, and 2.5. The dashed line denotes the minimum value of $\sigma_{sc} = 4e^2/\pi h$. Inset: comparison with self-consistent born approximation with fitting factor A=21 for W=2.

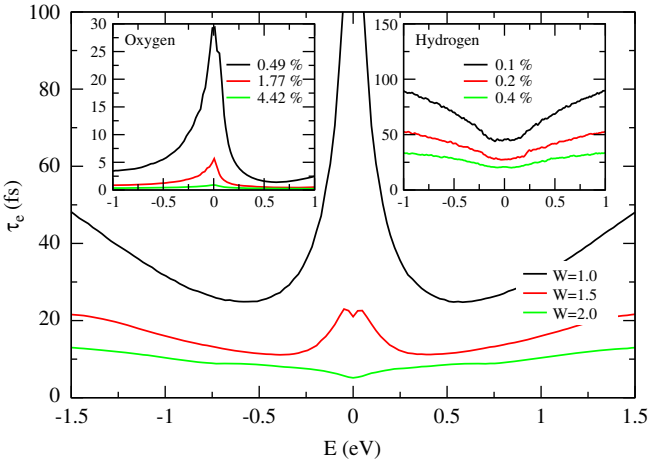

Fig. 2. (Color online) Elastic scattering time (τ_e) versus energy for three different Coulomb impurity potential strengths W. Left inset: τ_e for various densities of epoxide defects (adsorbed oxygen). Right inset: τ_e for various densities of hydrogen defects (sp^3 defects).

onsite energies at orbital α with $\varepsilon_\alpha = \sum_{i=1}^{N_I}\varepsilon_i \exp(-|\mathbf{r}_\alpha - \mathbf{r}_i|^2/(2\xi^2))$, where ξ defines the effective range, and ε_i are chosen at random within $[-W/2, W/2]\ \gamma_0$, where W denotes the strength of the local potential profile. Different random configurations of graphene samples with same size, ξ, W, and $n_i = N_i/N$ provide a statistical ensemble for a given disorder strength. We fix the impurity effective range $\xi = 3a = 0.426$ nm as a typical value for a long-range potential (a being the carbon–carbon distance), but vary W to describe different screening situations [53–55].

The impact of such type of disorder is actually strongly related to the value of W. In Fig. 2 (main frame), one shows the total elastic scattering time for three values of $W = 1.0, 1.5$ and 2.0 in γ_0 unit. Strikingly the behavior of $\tau_e(E)$ in the vicinity of the Dirac point is totally different. For W=2.0, its value saturates at $\tau_e(E=0) \approx 5$ fs, while it increases roughly linearly at higher energies. In sharp contrast, for W=1.5 and W=1.0 an upturn of τ_e is obtained close to the Dirac point followed by a saturation value of $\tau_e(E=0)$ (about 4 times larger for W=1.5) due to finite density of states. For the weakest disorder (W=1) we observe $\tau_e(E) \sim 1/E$ for low E and $\tau_e(E) \sim E$ for larger E.

This can be rationalized by a Fermi's golden rule calculation of the relaxation time taking the potential as a small perturbation.

Author's personal copy

Besides the energy dependence of the density of states, which we first assume being proportional to E, we get an additional energy dependent contribution for τ_e by Fourier transforming the long-range potential. For weak disorder the relaxation time for small energies can thus be approximated by $\tau_e \propto 1/E(1-cE^2) \approx 1/E+cE$ (focusing our discussion on the positive energy axis). Accordingly one would expect a low-energy peak and a linear slope at higher energies separated by a minimum τ_e at finite E (well away from the Dirac point). In the simulations such a weak disorder limit is nearly realized for $W=1.0$ as seen in Fig. 2, while for larger disorder the above estimation has to be modified to explain the results. Already for $W=1.5$ the DOS at the Dirac point is finite and the leading term for $\tau(E)$ at low-energy $1/E$, stemming from the DOS, is strongly reduced and regularized. As a result, the minimum for $\tau(E)$ still exists but is relocated to smaller energies ($E \approx 400$ meV). For stronger disorder ($W=2.0$) the DOS at the Dirac point is large enough that the minimum at finite E vanishes completely. In this case the zero-energy states relax fastest.

Next, to explore localization phenomena, we introduce a magnetic field through the Peierls phase [56], with a flux per hexagon given by $\phi = \oint \mathbf{A}\cdot d\mathbf{l} = h/e\sum_{\text{hexagon}}\varphi_{\alpha\beta}$. A gauge is implemented where $\sum_{\text{hexagon}}\varphi_{\alpha\beta}$ can take integer multiples of $1/(N_xN_y)$ with N_x and $N_y = N_x+1$ defining the sample size. The Landau levels obtained for clean graphene at $B=10$ Tesla follow the expected magnetic field dependent $\sqrt{nB}$ scaling (not shown here) [56].

The magnetoconductance $\Delta\sigma(B) = \sigma(B)-\sigma(B=0)$ is shown in the left panels of Figs. 3 and 4 for two different disorder strengths. For $W=2$ (Fig. 3), the sign of $\Delta\sigma(B)$ (positive magnetoconductance) evidences a weak-localization behavior, valid for various selected energies. In contrast, the case $W=1.5$ shows a clearly different behavior since a change in the sign of $\Delta\sigma(B)$ is observed, suggesting a crossover from weak localization to weak antilocalization, which depends not only on the field strength, but also on the considered energy of charge carriers. We note that an estimation of the elastic mean free path gives $\ell_e \sim 9-20$ nm, which is still much smaller than our sample size. Fig. 4 (right) gives the experimental results obtained by Tikhonenko and coworkers [10,11].

In Ref. [54], using the same long-range disorder potential, it was shown that valley mixing strength was continuously enhanced from $W=1$ to $W=2$ (with $\xi = 0.426$ nm). The positive magnetoconductance for the case $W=2$ agrees with the strong contribution of intervalley scattering, since all underlined symmetries have been broken. However by decreasing the disorder strength (from $W=2$ to $W=1.5$), WAL is indeed recovered given the reduction of intervalley processes. It is further instructive to related our simulations with the phenomenological law $\Delta\sigma(B) = e^2/\pi h\{\mathcal{F}(\tau_B^{-1}/\tau_\varphi^{-1})-3\mathcal{F}(\tau_B^{-1}/(\tau_\varphi^{-1}+2\tau_*^{-1}))\}$, where $\mathcal{F}(z) = \ln z+\psi(1/2+z^{-1})$, $\psi(x)$ is the digamma function and $\tau_B^{-1} = 4eDB/\hbar$ [9]. Good fits can be obtained using a single additional elastic (phenomenological) scattering time τ_* that contains both contributions of intravalley and intervalley scattering [9]. This is sounding since for the considered W values, both scattering processes actually compete and it is impossible to numerically disentangle individual contributions (see Ref. [54]). Least-squares fits (dashed lines) are superimposed to the simulated $\Delta\sigma(B)$

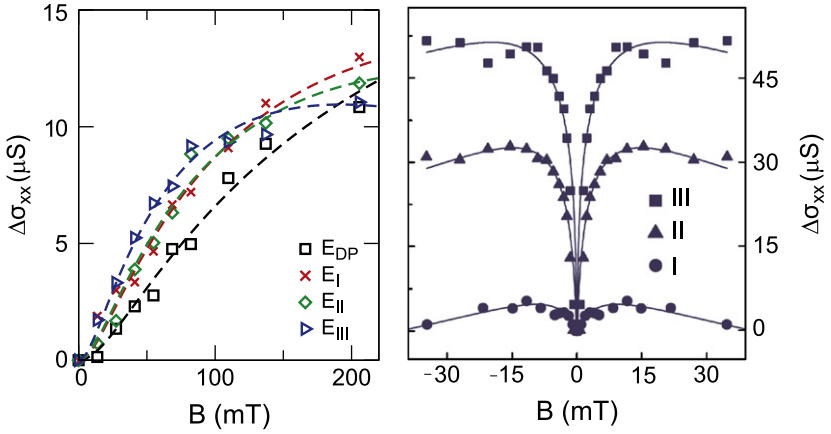

Fig. 3. (Color online) Left panel: $\Delta\sigma(B)$ ($n_i = 0.125\%$, $\xi = 0.426$ nm) for four different Fermi level positions ($E_{DP} = 0, E_I = 0.049$ eV, $E_{II} = 0.097$ eV and $E_{III} = 0.146$ eV). Averages over 32 different configurations are performed. Dashed lines are fits from analytical curves (see text). Right panel: experimental data extracted from [10,11].

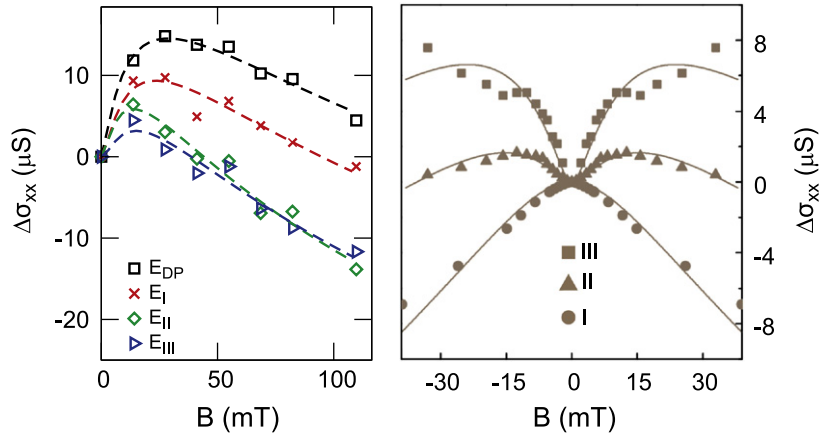

Fig. 4. (Color online) Left panel: $\Delta\sigma(B)$ for four different Fermi level positions ($E_{DP} = 0, E_I = 0.049$ eV, $E_{II} = 0.097$ eV and $E_{III} = 0.146$ eV) after Ref. [56]. 64 configurations have been averaged. Dashed lines are fits to analytical curves. Right panel: experimental data extracted from [10,11].

Author's personal copy

(symbols), taking $\tau_\varphi = 9$ ps (maximum computed time, which captures all coherent effects within this time scale). For $W=2$ and $W=1.5$, τ_* ranges within [1.1–2.3] ps and [1.5–6.3] ps, respectively (increasing values with increasing energy), thus confirming the weak localization regime for lowest B, which is fully consistent with Ref. [9] ($\tau_i < \tau_\varphi$).

It is thus shown that pseudospin effects can be actually tuned by adjusting a single disorder parameter (W) which denotes the depth of an impurity-driven local Coulomb potential. When $W \geq 1$ (unit of γ_0), local energetics between nearest neighbors A and B sites fluctuate enough to increase intervalley scattering which progressively predominate over the intravalley contribution [54].

4. Partly damaged graphene

4.1. Atomic oxygen case

Going to more realistic disorder models, the case of monoatomic oxygen atoms adsorbed on graphene in the so-called epoxy configuration is now scrutinized. A weak ozone treatment of the graphene sample can introduce such type of defects as discussed recently by Moser and coworkers [57].

It is worth noting that individual oxygen atoms find a very stable position when bridging two nearest neighbor carbon atoms. This bridge slightly displaces locations of both carbon atoms but does not yield a strongly covalent bond. To some extent, for a single epoxy defect, local AB symmetry is not broken (no notable local magnetic moments are found). To elaborate suitable tight-binding models for oxygen-damaged graphene, *ab initio* calculations are performed. These DFT calculations are conducted using the SIESTA code [58], within the local density approximation (LDA) on the exchange–correlation functional. From these calculations, a standard π electron orthogonal TB model with first nearest neighbors interactions of the p_x and the p_z orbitals of oxygen with carbon is derived. The combined contribution of the s and p_z orbitals of carbon binding with oxygen is simplified to a single orbital in this π-model. Practically, a $\sqrt{3}\times\sqrt{3}$ supercell with one epoxy atom is simulated to extract a DFT bandstructure with limited folding of the Brillouin zone. The bands near the Fermi energy are then nicely fitted using TB parameters. These parameters are confirmed for larger supercells (5×5) mimicking isolated adatoms. More details are given in Refs. [50,59].

Fig. 5 gives, for 4.42% epoxy defects, the σ_{sc} together with the quantum Kubo conductivity computed at different time scales (deep into the diffusive regime). These calculations are achieved by computing $D_x(E,t) = \partial(\Delta X^2(E,t))/\partial t$ and by evaluating $\sigma(E,t) = \frac{1}{4}e^2\rho(E)D(E,t)$. Oxygen defects produce quasibound states at some resonant energies which break the symmetry between electron and holes transport fingerprints close to the Dirac point. This asymmetry is already seen in the local density of states but further develops in the energy-dependence of $\ell_e(E)$, $\sigma_{sc}(E)$, and for all multiple scattering effects at the origin of localization effects [59].

The obtained time-evolution of the Kubo conductivity can be more precisely analyzed using the scaling theory of localization, since two different scalings behaviors are expected, namely the weak localization regime defined by

$$\sigma(L) - \sigma|_{D^{\max}} = -\frac{e^2}{\hbar\pi^2}\ln\left(\frac{L}{\sqrt{2}\ell_e}\right) \tag{2}$$

and the strong localization regime driven by

$$\sigma(L) \sim \exp\left(-\frac{L(t)}{\xi}\right) \tag{3}$$

where ξ denotes the localization length, while $L(t)$ is the length probed by the spreading of wavepacket at a given time t defined by $L(t) = 2\sqrt{2\Delta X^2(t)}$. The transition from the weak to the strong regime actually occurs when $k_F\ell_e = 1$ (Ioffe and Regel criterion [60]). For a defect density of 4.42%, $\ell_e \lesssim 3$ Å satisfies this criterion over the whole spectral window from 0.5 to 1 eV. It can be used to estimate ξ with the two-dimensional generalized version of the Thouless relationship $\xi(E) = \ell_e \exp(\pi\sigma_{sc}/G_0)$ [16]. On the other hand, ξ can be extracted from the exponential scaling decay of conductance with length.

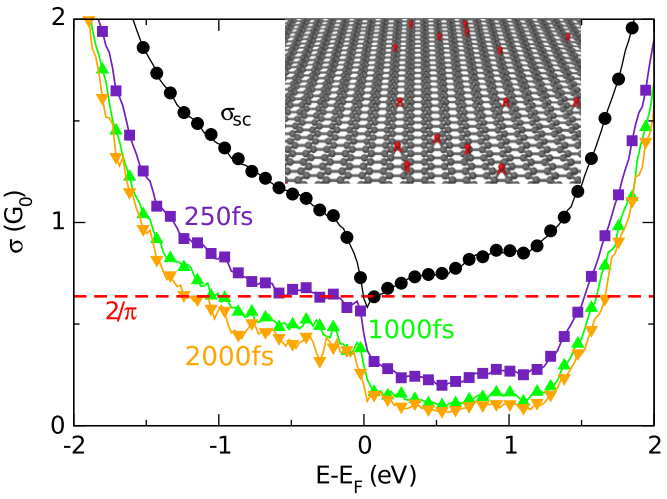

Fig. 5. (Color online) Main frame: Kubo conductivity at different times of wave packet evolution for 4.42% of impurities. The dashed line denotes the minimum value of $\sigma_{sc} = 4e^2/\pi h$. A ball and stick model of epoxy defects in graphene is shown in the inset.

Fig. 6 (main frame) shows that in the weak disorder limit (up to $\sim$1% of defects) both the numerical $\sigma(L)$ (symbols) and the analytical $\sigma_{D^{\max}} - e^2/\hbar\pi^2\ln(L/\sqrt{2}\ell_e)$ (solid lines) compare fairly well. The fitting becomes however much worst for larger defect density which suggests that the transport regime has been driven to the strong localization regime. Using the exponential scaling law, ξ values of 11.2 and 5.3 nm are respectively obtained for 3.22% and 4.42% of impurities (selected $E-E_F$ energy is 0.8 eV), consistent with prior estimation and in good agreement with experiment [57]. Using the Landauer–Büttiker method, the effect of epoxy defects on quantum transport in graphene nanoribbons has been shown to produce mobility gaps and much stronger electron–hole transport asymmetry [61].

4.2. Atomic hydrogen case

The adsorption of hydrogen atoms is of particular interest since it introduces sp^3 defects, which definitely break the AB symmetry and induces even more damage to the graphene lattice. Large hydrogen coverage might ultimately turns the material to a graphene insulator with large energy gap [62]. We are here interested in low hydrogen density limit, and in the regime for which the breaking of the AB sublattice symmetry is likely to induce local magnetic ordering as predicted by Lieb [63]. The study of magnetism in damaged graphene is endeavored using a self-consistent spin-dependent Hubbard Hamiltonian. In this model, the spin-related physics induced by Coulomb interaction is introduced by means of the Hubbard model in its mean-field approximation [33]

$$\mathcal{H} = \gamma_0 \sum_{\langle i,j\rangle,\sigma} c^\dagger_{i,\sigma}c_{j,\sigma} + U\sum_i n_{i,\uparrow}\langle n_{i,\downarrow}\rangle + n_{i,\downarrow}\langle n_{i,\uparrow}\rangle \tag{4}$$

where $c^\dagger_{i,\sigma}$ ($c_{j,\sigma}$) is the creation (annihilation) operator in the lattice site i (j) with spin σ, U is the on-site Coulomb repulsion, and $n_{i,\downarrow}$, $n_{i,\uparrow}$ are the self-consistent occupation numbers for spin-down and

Author's personal copy

spin-up electrons, respectively. The ratio U/t is chosen to reproduce spin density obtained from first-principles calculations. Kubo conductivity is now spin-dependent as $\sigma_{\uparrow,\downarrow}(E,t)=(e^2/2)\mathrm{Tr}[\delta_{\uparrow,\downarrow}(E-\hat{H})]D_{\uparrow,\downarrow}(E,t)$ with $\mathrm{Tr}[\delta_{\uparrow,\downarrow}(E-\hat{H})/S]$ and $D_{\uparrow,\downarrow}(E,t)$ are respectively the spin-dependent density of states per surface unit at Fermi energy E and the diffusion coefficients.

Fig. 7 (inset) shows $D_{\uparrow}(E,t)$ at three selected energies for $n_x=0.8\%$, assuming the hydrogen defects are distributed totally randomly through the graphene lattice (50% of hydrogen are distributed at random on each sublattices A and B). Similar results are obtained for the other (spin down) polarization. These diffusion coefficients reach a saturation regime after a few hundreds of femtoseconds, and then exhibit a strong logarithmic decay which is an unambiguous fingerprint of weak localization. The corresponding semiclassical and Kubo conductivities evaluated at long times are shown in Fig. 7 (main frame). As for the case of Anderson disorder, one notes that the Drude conductivity σ_{sc} remains larger than $4e^2/\pi h$, whereas as soon as quantum interferences come into play, $\sigma_{\uparrow,\downarrow}(E,t)$ becomes lower than its σ_{sc}, pinpointing the transition to a weak localization regime, depending on the considered length scale. This is illustrated in Fig. 7 (main frame) for two elapsed times $t=250$ fs and $t=2000$ fs.

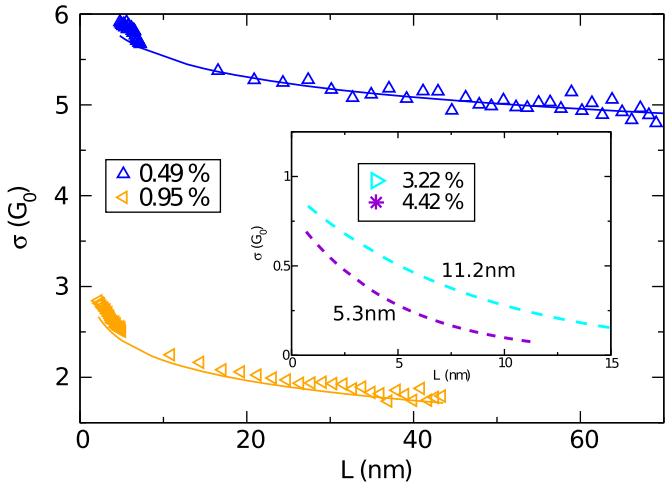

Fig. 6. (Color online) Kubo conductivities for L in the localized regimes for different impurity densities at energy 0.8 eV for weak defect concentration (main frame) (logarithmic behavior) and strong defect density (inset) (exponential behavior).

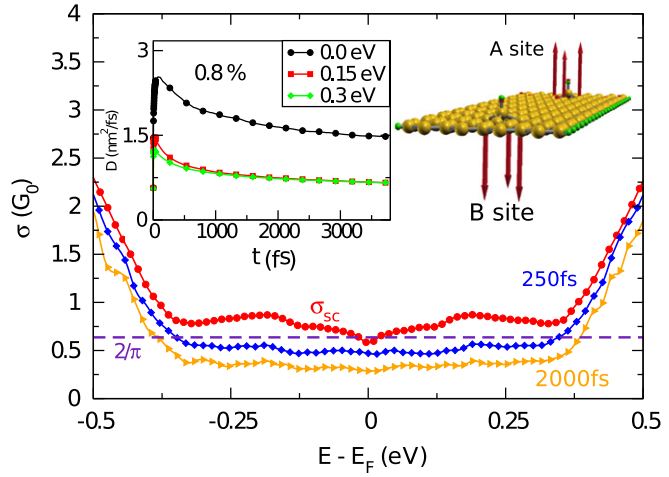

Fig. 7. (Color online) Main frame: Kubo conductivities for the non-magnetic state with $n_x=0.8\%$ hydrogen impurities. The values at D_{max} (extracted at $t=50$ fs) gives access to σ_{sc}, whereas values at longer elapsed times clearly evidence localization effects. The theoretical limit for σ_{sc} ($4e^2/h\pi$) is shown by the horizontal dashed line. Inset : corresponding time-dependent diffusion coefficients (spin up channel) for selected energies (see legends). Ball and stick model for two hydrogen defects with antiferromagnetic spin polarization (arrows) is also shown.

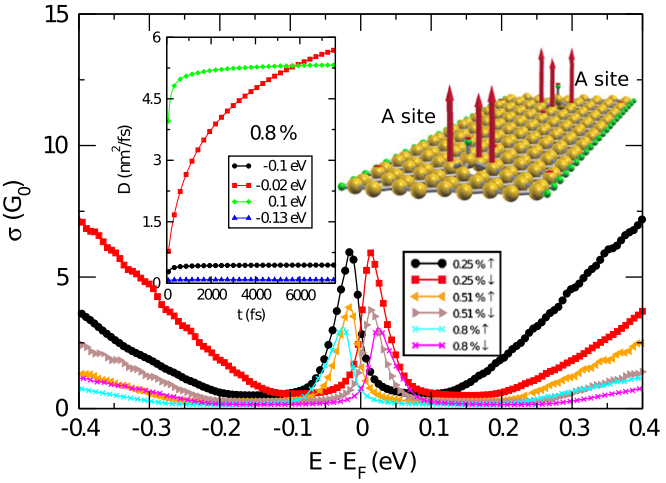

Fig. 8. (Color online) Kubo conductivities for the ferromagnetic AA magnetic state for different hydrogen coverages and for up and down spin configurations (elapsed time $t=7600$ fs). Inset: corresponding time-dependent diffusion coefficients (spin up channel) for selected energies (see legends). Ball and stick model for two hydrogen defects with ferromagnetic spin polarization (arrows) is also shown.

In striking contrast, if hydrogen defects are placed at random but restricted to one of the two sublattices (say sublattice A for illustration), transport properties become totally different. This is shown in Fig. 8 (inset) where the diffusion coefficient are indeed seen to reach saturation at enough long time but without any further decay. This also is evident from the conductivity which saturates to its semiclassical value, pinpointing the total suppression of quantum interferences and localization effects (Fig. 8, main frame). The preservation of one of the sublattice free from sp^3 defects maximizes the existence of local ferromagnetic ordering and also introduces restrictions for multiple scattering events. This therefore establishes a deep connection between the existence of a ferromagnetic order and a robust metallic state down to zero temperature. We outline that our disorder model preserves the chiral (electron-hole) symmetry [52], which has theoretically been shown to drive either logarithmic increase (for resonant scatterers) or saturation (for vacancies) of the conductivity [67]. Puzzling magnetoresistance experiments in dilute fluorinated graphene were also recently discussed in the frame of interplay between local magnetism ordering and localization effects [64].

4.3. Scattering times

It is also finally worth to discuss the various behaviors of elastic scattering times, depending on the nature of underlying disorders. In Fig. 2, elastic scattering times versus energy (τ_e) are shown for varying oxygen (left inset) and hydrogen ad-atoms (right inset) densities. It is worth to note that the epoxide defects which actually preserve some local AB symmetry also induce energy-dependent $\tau_e(E)$ ressembling the case of long rang Coulomb impurities with onsite potential depth ($W=1.5$, Fig. 2, main frame). Differently, the $\tau_e(E)$ fingerprint of hydrogen defects which break local sp^2 symmetry and local AB degeneracy is more ressembling the case $W=2$. We also note that such energy-dependence of scattering times are weakly dependent on the defect density but mostly driven by structural re-arrangements and local symmetry breaking, although similar defect density leads to equivalent $\tau_e(E)$ at the Dirac point (in the order of 25–30

Author's personal copy

fs for $n_i \simeq 0.4\%$, see insets in Fig. 2). These features should be useful to better rationalize the possible nature of defects in different graphene-based materials (see Refs. [65,66] for some experimental discussion).

5. Conclusions

In conclusion, quantum transport phenomena in disordered graphene have been discussed for several types of disorder models. Based on the Anderson disorder potential or long range Coulomb impurities we have first validated well established analytical results such as the minimum semiclassical conductivity at Dirac point, and the possibility to obtain crossover between weak localization to weak antilocalization depending on the disorder characteristics in full agreement with diagrammatic theory and experiments.

More realistic models of damaged graphene with oxygen and hydrogen defects have been studied. The scaling theory of localization (and transition from weak to strong localization) has been illustrated with varying density of epoxy defects, whereas grafted atomic hydrogen atoms have been shown to open the possibility to crosslink the existence of local ferromagnetic ordering with the absence of localization effects down to vanishing temperatures, a fact quite unique in graphene and deserving further experimental inspection.

The comparison of elastic scattering times for different disorder sources has also been instructive, showing that the low-energy dependence of τ_e is driven by local disorder potential fluctuations which partly or totally break underlying symmetries. This could serve as guidance for rationalizing the source of disorder in measured samples.

Acknowledgments

We thank P. Ordejon, J.J. Palacios, J. Fernandez-Rossier and G. Montambaux for fruitful discussions. J.-C.C., N.L., and A.L. acknowledge financial support from the F.R.S.-FNRS of Belgium. This work is directly connected to the Belgian Program on Interuniversity Attraction Poles (PAI6) on Quantum Effects in Clusters and Nanowires, to the ARC on Graphene StressTronics sponsored by the Communauté Française de Belgique, to the European Union through the ETSF e-I3 project (Grant nr 211956), and to the NANOSIM-GRAPHENE project (Projet nr ANR-09-NANO-016-01). Computational resources were provided by the CISM of the Université catholique de Louvain: several numerical simulations have been performed on the GREEN and LEMAITRE computers of the CISM. F.O. would like to thank the European Commission for a Marie Curie Fellowship.

References

[1] K.S. Novoselov, A.K. Geim, S.V. Morozov, D. Jiang, Y. Zhang, S.V. Dubonos, I.V. Grigorieva, A.A. Firsov, Science 306 (2004) 666.
[2] K.S. Novoselov, A.K. Geim, S.V. Morozov, D. Jiang, M.I. Katsnelson, I.V. Grigorieva, S.V. Dubonos, A.A. Firsov, Nature (London) A38 (2005) 197.
[3] K.S. Novoselov, Rev. Mod. Phys. 83 (2011) 837.
[4] D.S.L. Abergel, V. Apalkov, J. Berashevich, K. Ziegler, T. Chakraborty, Adv. Phys. 59 (2010) 261.
[5] A. Cresti, N. Nemec, B. Biel, G. Niebler, F. Triozon, G. Cuniberti, S. Roche, Nano Res. 1 (2008) 361.
[6] F. Schwierz, Nat. Nanotechnol. 5 (2010) 487.
[7] M.I. Katsnelson, K.S. Novoselov, A.K. Geim, Nat. Phys. 2 (2006) 620.
[8] C.-H. Park, Y.W. Son, L. Yang, M.L. Cohen, S.G. Louie, Nano Lett. 8 (2008) 2920.
[9] E. McCann, K. Kechedzhi, V.I. Falko, H. Suzuura, T. Ando, B.L. Altshuler, Phys. Rev. Lett. 97 (2006) 146805.
[10] F.V. Tikhonenko, D.W. Horsell, R.V. Gorbachev, A.K. Savchenko, Phys. Rev. Lett. 100 (2008) 056802.
[11] F.V. Tikhonenko, A.A. Kozikov, A.K. Savchenko, R.V. Gorbachev, Phys. Rev. Lett. 103 (2009) 226801.
[12] K.S. Novoselov, A.K. Geim, S.V. Morozov, D. Jiang, M.I. Katsnelson, I.V. Grigorieva, S.V. Dubonos, A.A. Firsov, Nature 438 (2005) 197.
[13] Y.B. Zhang, Y.-W. Tan, H.L. Stormer, Ph. Kim, Nature 438 (2005) 201.
[14] A. Lherbier, X. Blase, Y.M. Niquet, F. Triozon, S. Roche, Phys. Rev. Lett. 101 (2008) 036808.
[15] B. Biel, F. Triozon, X. Blase, S. Roche, Nano Lett. 9 (2009) 2725.
[16] P.A. Lee, T.V. Ramakrishnan, Rev. Mod. Phys. 57 (1985) 2.
[17] S. Hikami, A.I. Larkin, Y. Nagaoka, Prog. Theor. Phys. 63 (1980) 707.
[18] G. Bergman, Phys. Rev. Lett. 48 (1982) 1046.
[19] H. Suzuura, T. Ando, Phys. Rev. Lett. 89 (2002) 266603.
[20] A. Altland, Phys. Rev. Lett. 97 (2006) 236802.
[21] I.L. Aleiner, K.B. Efetov, Phys. Rev. Lett. 97 (2006) 236801.
[22] J.H. Bardarson, J. Tworzydlo, P.W. Brouwer, C.W.J. Beenakker, Phys. Rev. Lett. 99 (2007) 106801.
[23] K. Nomura, M. Koshino, S. Ryu, Phys. Rev. Lett. 99 (2007) 146806.
[24] A. Lherbier, S.M.-M. Dubois, X. Declerck, S. Roche, Y.M. Niquet, J.-C. Charlier, Phys. Rev. Lett. 106 (2011) 046803.
[25] P.M. Ostrovsky, M. Titov, S. Bera, I.V. Gornyi, A.D. Mirlin, Phys. Rev. Lett. 105 (2010) 266803.
[26] M. Titov, P.M. Ostrovsky, A. Schuessler, I.V. Gornyi, A.D. Mirlin, Phys. Rev. Lett. 104 (2010) 07680.
[27] S. Yuan, R. Roldan, H. de Raedt, M.I. Katsnelson, Phys. Rev. B 84 (2011) 195418-1.
[28] G. Trambly de Laissardiere, D. Mayou, Mod. Phys. Lett. B 25 (2011) 1019.
[29] J. Kotakoski, A.V. Krasheninnikov, U. Kaiser, J.C. Meyer, Phys. Rev. Lett. 106 (2011) 105505.
[30] D.C. Elias, R. Nair, T. Mohiuddin, S. Morozov, P. Blake, M. Halsall, A. Ferrari, D. Boukhvalov, M. Katsnelson, A. Geim, K. Novoselov, Science 323 (2009) 610.
[31] C. Gómez-Navarro, R.T. Weitz, A.M. Bittner, M. Scolari, A. Mews, M. Burghard, K. Kern, Nano Lett. 7 (2007) 3499.
[32] F. Evers, A.D. Mirlin, Rev. Mod. Phys. 80 (2008) 1355.
[33] D. Soriano, N. Leconte, P. Ordejon, J.-C. Charlier, J.-J. Palacios, S. Roche, Phys. Rev. Lett. 107 (2011) 16602.
[34] L.A. Ponomarenko, A.A. Zhukov, R. Jalil, S.V. Morozov, K.S. Novoselov, V.V. Cheianov, V.I. Falko, K. Watanabe, T. Taniguchi, A.K. Geim, R.V. Gorbachev, Nat. Phys. 7 (2011) 958.
[35] S. Roche, D. Mayou, Phys. Rev. Lett. 79 (1997) 2518.
[36] S. Roche, Phys. Rev. B 59 (1999) 2284.
[37] S. Roche, R. Saito, Phys. Rev. Lett. 87 (2001) 246803.
[38] F. Triozon, S. Roche, A. Rubio, D. Mayou, Phys. Rev. B 69 (2004) 121410(R).
[39] H. Ishii, F. Triozon, N. Kobayashi, K. Hirose, S. Roche, C. R. Phys. 10 (2009) 283.
[40] S. Latil, S. Roche, D. Mayou, J.-C. Charlier, Phys. Rev. Lett. 92 (2004) 256805.
[41] A. Lherbier, B. Biel, Y.-M. Niquet, S. Roche, Phys. Rev. Lett. 100 (2008) 036803.
[42] R. Haydock, V. Heine, M.J. Kelly, J. Phys. C 5 (1972) 2845.
[43] H. Sevincli, W. Li, N. Mingo, G. Cuniberti, S. Roche, Phys. Rev. B 84 (2011) 205444.
[44] W. Li, H. Sevincli, S. Roche, G. Cuniberti, Phys. Rev. B 83 (2011) 155416.
[45] W. Li, H. Sevincli, G. Cuniberti, S. Roche, Phys. Rev. B. 82 (2010) 041410(RC).
[46] T. Ando, R. Saito, T. Nakanishi, J. Phys. Soc. Jpn. 67 (1998) 2857.
[47] C.T. White, T.N. Todorov, Nature (London) 393 (1998) 240.
[48] S. Roche, R. Saito, G. Dresselhaus, M. Dresselhaus, Phys. Rev. B. 62 (2000) 16092.
[49] J.C. Charlier, X. Blase, S. Roche, Rev. Mod. Phys. 79 (2007) 677.
[50] N. Leconte, J. Moser, P. Ordejon, H. Tao, A. Lherbier, A. Bachtold, F. Alsina, C.M. Sotomayor Torres, J.C. Charlier, S. Roche, ACS Nano 4 (2010) 4033–4038.
[51] N.H. Shon, T. Ando, J. Phys. Soc. Jpn. 67 (1998) 2421.
[52] P.M. Ostrovsky, I.V. Gornyi, A.D. Mirlin, Phys. Rev. B 74 (2006) 235443.
[53] K. Nomura, A.H. MacDonald, Phys. Rev. Lett. 98 (2007) 076602.
[54] Y.Y. Zhang, J. Hu, B.A. Bernevig, X.R. Wan, X.C. Xie, W.M. Liu, Phys. Rev. Lett. 102 (2009) 106401.
[55] S. Das Sarma, S. Adam, E.H. Hwang, E. Rossi, Rev. Mod. Phys. 83 (2011) 407–470.
[56] F. Ortmann, A. Cresti, G. Montambaux, S. Roche, Europhys. Lett. 94 (2011) 47006.
[57] J. Moser, H. Tao, S. Roche, F. Alsina, C.M. Sotomayor Torres, A. Bachtold, Phys. Rev. B 81 (2010) 205445.
[58] J.M. Soler, E. Artacho, J.D. Gale, A. Garcia, J. Junquera, P. Ordejon, D. Sanchez-Portal, J. Phys.: Condens. Matter 14 (2002) 2745.
[59] N. Leconte, A. Lherbier, F. Varchon, P. Ordejon, S. Roche, J.-C. Charlier, Phys. Rev. B 84 (2011) 235420.
[60] A.F. Ioffe, A.R. Regel, Prog. Semicond. 4 (1960) 237.
[61] A. Cresti, A. Lopez-Bezanilla, P. Ordejon, S. Roche, ACS Nano 5 (2011) 9271.
[62] D.C. Elias, R.R. Nair, T.M.G. Mohiuddin, S.V. Morozov, P. Blake, M. P Halsall, A.C. Ferrari, D.W. Boukhvalov, M.I. Katsnelson, A.K. Geim, K.S. Novoselov, Science 323 (2009) 610.
[63] E.H. Lieb, Phys. Rev. Lett. 62 (1989) 1201.
[64] X. Hong, S.-H. Cheng, C. Herding, J. Zhu, Phys. Rev. B 83 (2011) 085410.
[65] M. Monteverde, C. Ojeda-Aristizabal, R. Weil, K. Bennaceur, M. Ferrier, S. Gueron, C. Glattli, H. Bouchiat, J.N. Fuchs, D.L. Maslov, Phys. Rev. Lett. 104 (2010) 126801.
[66] X. Hong, K. Zou, J. ZHu, Phys. Rev. B 80 (2009) 241415.
[67] P.M. Ostrovsky, M. Titov, S. Bera, L.V. Gornyi, A.D. Mirlin, Phys. Rev. Lett. 105 (2010) 266803.